THE 2014 ALMA LONG BASELINE CAMPAIGN: AN OVERVIEW*

ALMA PARTNERSHIP, E. B. FOMALONT[1,2], C. VLAHAKIS[1,3], S. CORDER[1,2], A. REMIJAN[1,2], D. BARKATS[1,3], R. LUCAS[4],
T. R. HUNTER[2], C. L. BROGAN[2], Y. ASAKI[5,6], S. MATSUSHITA[7], W. R. F. DENT[1,3], R. E. HILLS[8], N. PHILLIPS[1,3], A. M. S. RICHARDS[9],
P. COX[1,3], R. AMESTICA[2], D. BROGUIERE[10], W. COTTON[2], A. S. HALES[1,2], R. HIRIART[11], A. HIROTA[1,5], J. A. HODGE[2],
C. M. V. IMPELLIZZERI[1,2], J. KERN[11], R. KNEISSL[1,3], E. LIUZZO[12], N. MARCELINO[12], R. MARSON[11], A. MIGNANO[12],
K. NAKANISHI[1,5], B. NIKOLIC[8], J. E. PEREZ[2], L. M. PÉREZ[11], I. TOLEDO[1], R. ALADRO[3], B. BUTLER[2], J. CORTES[1,2], P. CORTES[1,2],
V. DHAWAN[11], J. DI FRANCESCO[13], D. ESPADA[1,5], F. GALARZA[1], D. GARCIA-APPADOO[1,3], L. GUZMAN-RAMIREZ[3],
E. M. HUMPHREYS[14], T. JUNG[15], S. KAMENO[1,5], R. A. LAING[14], S. LEON[1,3], J. MANGUM[2], G. MARCONI[1,3], H. NAGAI[5],
L.-A. NYMAN[1,3], M. RADISZCZ[1], J. A. RODÓN[3], T. SAWADA[1,5], S. TAKAHASHI[1,5], R. P. J. TILANUS[16], T. VAN KEMPEN[16],
B. VILA VILARO[1,3], L. C. WATSON[3], T. WIKLIND[1,3], F. GUETH[10], K. TATEMATSU[5], A. WOOTTEN[2], A. CASTRO-CARRIZO[10],
E. CHAPILLON[10,17,18], G. DUMAS[10], I. DE GREGORIO-MONSALVO[1,3], H. FRANCKE[1], J. GALLARDO[1], J. GARCIA[1], S. GONZALEZ[1],
J. E. HIBBARD[2], T. HILL[1,3], T. KAMINSKI[3], A. KARIM[19], M. KRIPS[10], Y. KURONO[1,5], C. LOPEZ[1], S. MARTIN[10], L. MAUD[16],
F. MORALES[1], V. PIETU[10], K. PLARRE[1], G. SCHIEVEN[13], L. TESTI[14], L. VIDELA[1], E. VILLARD[1,3], N. WHYBORN[1,3], M. A. ZWAAN[14],
F. ALVES[20], P. ANDREANI[14], A. AVISON[9], M. BARTA[21], F. BEDOSTI[12], G. J. BENDO[9], F. BERTOLDI[19], M. BETHERMIN[14], A. BIGGS[14],
J. BOISSIER[10], J. BRAND[12], S. BURKUTEAN[19], V. CASASOLA[22], J. CONWAY[23], L. CORTESE[24], B. DABROWSKI[25], T. A. DAVIS[26],
M. DIAZ TRIGO[14], F. FONTANI[22], R. FRANCO-HERNANDEZ[27], G. FULLER[9], R. GALVAN MADRID[28], A. GIANNETTI[19], A. GINSBURG[14],
S. F. GRAVES[8], E. HATZIMINAOGLOU[14], M. HOGERHEIJDE[16], P. JACHYM[21], I. JIMENEZ SERRA[14], M. KARLICKY[21], P. KLAASEN[16],
M. KRAUS[21], D. KUNNERIATH[21], C. LAGOS[14], S. LONGMORE[14], S. LEURINI[29], M. MAERCKER[23], B. MAGNELLI[19], I. MARTI VIDAL[23],
M. MASSARDI[12], A. MAURY[31], S. MUEHLE[19], S. MULLER[29], T. MUXLOW[9], E. O'GORMAN[29], R. PALADINO[12], D. PETRY[14],
J. PINEDA[20], S. RANDALL[14], J. S. RICHER[8], A. ROSSETTI[12], A. RUSHTON[32], K. RYGL[12], A. SANCHEZ MONGE[33], R. SCHAAF[19],
P. SCHILKE[33], T. STANKE[14], M. SCHMALZL[16], F. STOEHR[14], S. URBAN[21], E. VAN KAMPEN[14], W. VLEMMINGS[23], K. WANG[14],
W. WILD[14], Y. YANG[15], S. IGUCHI[5], T. HASEGAWA[5], M. SAITO[5], J. INATANI[5], N. MIZUNO[1,5], S. ASAYAMA[5], G. KOSUGI[5],
K.-I. MORITA[1,5], K. CHIBA[5], S. KAWASHIMA[5], S. K. OKUMURA[34], N. OHASHI[5], R. OGASAWARA[5], S. SAKAMOTO[5], T. NOGUCHI[5],
Y.-D. HUANG[7], S.-Y. LIU[7], F. KEMPER[7], P. M. KOCH[7], M.-T. CHEN[7], Y. CHIKADA[5], M. HIRAMATSU[5], D. IONO[5], M. SHIMOJO[5],
S. KOMUGI[5,35], J. KIM[15], A.-R. LYO[15], E. MULLER[5], C. HERRERA[5], R. E. MIURA[5], J. UEDA[5], J. CHIBUEZE[5,36], Y.-N. SU[7],
A. TREJO-CRUZ[7], K.-S. WANG[7], H. KIUCHI[5], N. UKITA[5], M. SUGIMOTO[1,5], R. KAWABE[5], M. HAYASHI[5], S. MIYAMA[37,38], P. T. P. HO[7],
N. KAIFU[5], M. ISHIGURO[5], A. J. BEASLEY[2], S. BHATNAGAR[11], J. A. BRAATZ III[2], D. G. BRISBIN[2], N. BRUNETTI[2], C. CARILLI[11],
J. H. CROSSLEY[2], L. D'ADDARIO[39], J. L. DONOVAN MEYER[2], D. T. EMERSON[2], A. S. EVANS[2,40], P. FISHER[2], K. GOLAP[11],
D. M. GRIFFITH[2], A. E. HALE[2], D. HALSTEAD[2], E. J. HARDY[41,27], M. C. HATZ[2], M. HOLDAWAY[2], R. INDEBETOUW[2,40], P. R. JEWELL[2],
A. A. KEPLEY[2], D.-C. KIM[2], M. D. LACY[2], A. K. LEROY[2], H. S. LISZT[2], C. J. LONSDALE[2], B. MATTHEWS[13], M. MCKINNON[2],
B. S. MASON[2], G. MOELLENBROCK[11], A. MOULLET[2], S. T. MYERS[11], J. OTT[11], A. B. PECK[2], J. PISANO[2], S. J. E. RADFORD[42],
W. T. RANDOLPH[2], U. RAO VENKATA[11], M. G. RAWLINGS[2], R. ROSEN[2], S. L. SCHNEE[2], K. S. SCOTT[2], N. K. SHARP[2], K. SHETH[2],
R. S. SIMON[2], T. TSUTSUMI[11], AND S. J. WOOD[2]
[1] Joint ALMA Observatory, Alonso de Córdova 3107, Vitacura, Santiago, Chile; efomalon@nrao.edu
[2] National Radio Astronomy Observatory, 520 Edgemont Road, Charlottesville, VA 22903, USA
[3] European Southern Observatory, Alonso de Córdova 3107, Vitacura, Santiago, Chile
[4] Institut de Planétologie et d'Astrophysique de Grenoble (UMR 5274), BP 53, F-38041 Grenoble Cedex 9, France
[5] National Astronomical Observatory of Japan, 2-21-1 Osawa, Mitaka, Tokyo 181-8588, Japan
[6] Institute of Space and Astronautical Science (ISAS), Japan Aerospace Exploration Agency (JAXA),
3-1-1 Yoshinodai, Chuo-ku, Sagamihara, Kanagawa 252-5210 Japan
[7] Institute of Astronomy and Astrophysics, Academia Sinica, P.O. Box 23-141, Taipei 106, Taiwan
[8] Astrophysics Group, Cavendish Laboratory, JJ Thomson Avenue, Cambridge CB3 0HE, UK
[9] Jodrell Bank Centre for Astrophysics, School of Physics and Astronomy, University of Manchester, Oxford Road, Manchester M13 9PL, UK
[10] Institut de Radioastronomie Millimétrique (IRAM), 300 rue de la Piscine, Domaine Universitaire, F-38406 Saint Martin d'Hères, France
[11] National Radio Astronomy Observatory, P.O. Box O, Socorro, NM 87801, USA
[12] INAF, Istituto di Radioastronomia, via P. Gobetti 101, I-40129 Bologna, Italy
[13] National Research Council Herzberg Astronomy & Astrophysics, 5071 West Saanich Road, Victoria, BC V9E 2E7, Canada
[14] European Southern Observatory, Karl-Scshwarzschild-Strasse 2, D-85748 Garching bei München, Germany
[15] Korea Astronomy and Space Science Institute, Daedeokdae-ro 776, Yuseong-gu, Daejeon 305-349, Korea
[16] Leiden Observatory, Leiden University, P.O. Box 9513, 2300 RA Leiden, The Netherlands
[17] Univ. Bordeaux, LAB, UMR 5804, F-33270 Floirac, France
[18] CNRS, LAB, UMR 5804, F-33270 Floirac, France
[19] Argelander-Institut für Astronomie, Universität Bonn, Auf dem Hügel 71, D-53121 Bonn, Germany
[20] Max Planck Institute for Extraterrestial Physics, Giessenbachstr. 1, D-85748 Garching, Germany
[21] Astronomical Institute of the Academy of Sciences of the Czech Republic, 25165 Ondrejov, Czech Republic
[22] INAF-Oss. Astrofisco di Arcetri, Florence, Italy
[23] Department of Earth and Space Sciences, Chalmers University of Technology, Onsala Space Observatory, SE-439 92 Onsala, Sweden
[24] Centre for Astrophysics & Supercomputing, Swinburne University of Technology, Mail H30, P.O. Box 218, Hawthorn, VIC 3122, Australia
[25] Space Radio-diagnostics Research Center, Geodesy and Land Management,University of Warmia and Mazury, Olsztyn, Poland
[26] Centre for Astrophysics Research, Science & Technology Research Institute, University of Hertfordshire, Hatfield AL10 9AB, UK
[27] Departamento de Astronomía, Universidad de Chile, Casilla 36-D, Santiago, Chile
[28] Centro de Radiostronomía y Astrofísica, Universidad Nacional Autónoma de México, 58089 Morelia, Michoacán, México

[29] Max-Planck-Institut für Radioastronomie, Auf dem Hügel 69, D-53121 Bonn, Germany

[30] Astrophysics Research Institute, Liverpool John Moores University, IC2, Liverpool Science Park, 146 Brownlow Hill, Liverpool L3 5RF, UK

[31] Laboratoire AIM, CEA/DSM-CNRS-Université Paris Diderot, IRFU/Service dAstrophysique, Saclay, F-91191 Gif-sur-Yvette, France

[32] Department of Physics, Astrophysics, University of Oxford, Keble Road, Oxford OX1 3RH, UK

[33] I. Physikalisches Institut, Universität zu Köln, Zülpicher Str. 77, 50937, Köln, Germany

[34] Faculty of Science, Japan Women's University, 2-8-1 Mejirodai, Bunkyo-ku, Tokyo 112-8681, Japan

[35] Kogakuin University, 2665-1 Nakano-machi, Hachioji-shi, Tokyo 192-0015, Japan

[36] Department of Physics & Astronomy, University of Nigeria, Carver Building, Nsukka 410001, Nigeria

[37] National Institutes of Natural Sciences (NINS), 2 F Hulic Kamiyacho Building, 4-3-13 Toranomon, Minato-ku, Tokyo, Japan

[38] Hiroshima Astrophysical Science Center, Hiroshima University, 1-3-1 Kagamiyama, Higashi-Hiroshima, Hiroshima 739-8526, Japan

[39] Jet Propulsion Laboratory, California Institute of Technology, 4800 Oak Grove Drive, Pasadena, CA 91109, USA

[40] Department of Astronomy, University of Virginia, P.O. Box 3818, Charlottesville, VA 22903, USA

[41] National Radio Astronomy Observatory, Avenida Nueva Costanera 4091, Vitacura, Santiago, Chile

[42] Cahill Center for Astronomy and Astrophysics, California Institute of Technology, 1200 E. California Boulevard, M/C 249-17, Pasadena, CA 91125, USA

ABSTRACT

A major goal of the Atacama Large Millimeter/submillimeter Array (ALMA) is to make accurate images with resolutions of tens of milliarcseconds, which at submillimeter (submm) wavelengths requires baselines up to ~15 km. To develop and test this capability, a Long Baseline Campaign (LBC) was carried out from 2014 September to late November, culminating in end-to-end observations, calibrations, and imaging of selected Science Verification (SV) targets. This paper presents an overview of the campaign and its main results, including an investigation of the short-term coherence properties and systematic phase errors over the long baselines at the ALMA site, a summary of the SV targets and observations, and recommendations for science observing strategies at long baselines. Deep ALMA images of the quasar 3C 138 at 97 and 241 GHz are also compared to VLA 43 GHz results, demonstrating an agreement at a level of a few percent. As a result of the extensive program of LBC testing, the highly successful SV imaging at long baselines achieved angular resolutions as fine as 19 mas at ~350 GHz. Observing with ALMA on baselines of up to 15 km is now possible, and opens up new parameter space for submm astronomy.

Key words: instrumentation: interferometers – submillimeter: general – techniques: high angular resolution – techniques: interferometric – telescopes

1. INTRODUCTION

The Atacama Large Millimeter/submillimeter Array (ALMA) is a millimeter/submillimeter (mm/submm) interferometer located in the Atacama desert of northern Chile at an elevation of about 5000 m above sea level. The high-altitude, dry site provides excellent atmospheric transmission over the frequency range 85–900 GHz (Matsushita et al. 1999). ALMA is currently in its third year of science operations and was formally inaugurated in 2013 March. Until now, science observations have used configurations with baselines from 100 m to ~1.5 km, with some limited testing of a ~3 km baseline in 2013 (Asaki et al. 2014; Matsushita et al. 2014).

To test the highest angular resolution capability of ALMA using baseline lengths of up to ~15 km at selected frequencies, the three-month period from 2014 September to November was dedicated to carrying out the 2014 ALMA Long Baseline Campaign (LBC).[43] The approximate resolutions that can be achieved with the longest baselines are 60 mas at 100 GHz, 25 mas at 250 GHz and 17 mas at 350 GHz (but these can vary by ~20% depending on the imaging parameters). The major goal of the campaign was to develop the technical capabilities and procedures needed in order to offer ALMA long baseline array configurations for future science observations.

This paper presents an overview of the ALMA LBC, focusing on the technical issues affecting submm interferometry on baselines longer than a few kilometers. In Section 2, we describe the LBC array and campaign test strategy. Section 3 describes the effects of short-term phase variation due to the atmosphere and a method for determining if conditions are sufficiently stable for imaging. In Section 4, we discuss the systematic phase errors found between the calibrator and science target. In Section 5, an overview of Science Verification (SV) at long baselines is given. Images and initial science results on the SV targets are presented in three accompanying papers (ALMA Partnership et al. 2015a, 2015b, 2015c, hereafter ALMA II, ALMA III, ALMA IV, respectively). An illustration of the quality of the ALMA calibration and imaging is given by a comparison of preliminary ALMA SV and Very Large Array (VLA) images of 3C 138 with the same resolution (Appendix A). In Section 6, we present conclusions drawn from the LBC and recommendations for science observing using long baselines with ALMA.

2. LBC OVERVIEW

2.1. The LBC Array

Since many of the distant antenna pads had not been previously powered or occupied, a coordinated effort was made from 2014 April to August to prepare a sufficient number of antenna stations beyond 2 km from the array center. The configuration process began with an initial test in late 2014 August when a single antenna was moved out to a 7 km baseline. The nominal LBC configuration consisted of 21–23 antennas on baselines of between 400 m and 15 km and was

---
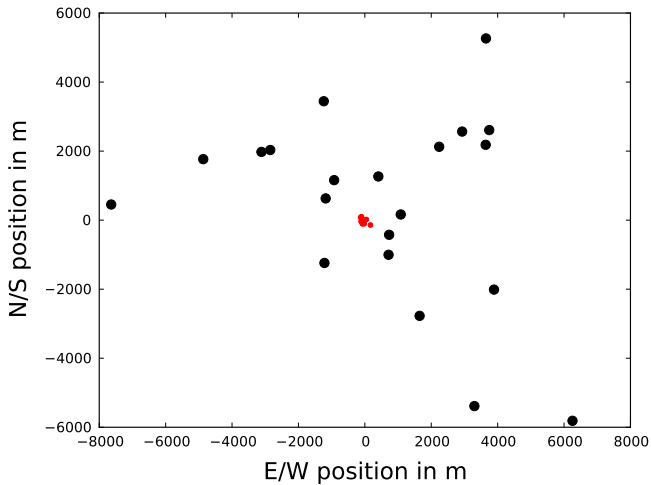
Figure 1. Example LBC array configuration (in this case the array that was used for the 3C 138 Band 6 observations in Appendix A). The black points show the nominal LBC antennas. The five antennas near the center (red points) are not part of the nominal LBC array, but were useful for measuring more extended emission (the number of these antennas varied; see Section 2 for details). The axis units are in meters.

Figure 2. *uv* distribution for the ∼1 hr 3C 138 Band 6 observations. The *u*-axis is the east–west spacing and the *v*-axis is the north–south spacing. The axis units are in kilo-lambda (kλ, where 1000 kλ = 1300 m).

available from the end of 2014 September until mid-November (with the two longest baseline antennas being added in mid-October). In addition, typically 6–12 antennas were available on baselines less than 300 m that were useful for imaging the more extended sources (though since they were not part of the nominal LBC configuration, the number of these antennas on short spacings varied from day to day and with observing Band). Thus, the total number of antennas used during the campaign typically ranged from 22 to 36, depending on observing date and observing Band. An example configuration used during the campaign (in this case for the SV observations of 3C 138; see Appendix A) is shown in Figure 1. The resultant *uv*-coverage for a ∼1-hr observation of 3C 138 with this array is shown in Figure 2.

2.2. LBC Test Strategy

The normal calibration mode for ALMA observing is phase referencing (Beasley & Conway 1995). Over the length of an experiment that can last for several hours, this observing mode alternates short scans of the science target and a nearby quasar that is used to calibrate the target data. Hence, the outcome of the long baseline observations depends strongly on the accuracy with which the phase measured on the calibrator can be transferred to the target. The LBC concentrated on the accuracy of this transfer by (1) performing test observations of quasars to establish the properties of the phase coherence of the array over long baselines; (2) determining how to optimize observing strategy to achieve good imaging results; and (3) observing, calibrating, and imaging SV targets and other test targets to demonstrate the end-to-end capability of ALMA long baseline observations.

Key plans for the LBC testing included: (1) *source stares*: 30 minute observations of a single bright source to determine the temporal phase variation statistics as a function of baseline length; (2) *short phase reference tests*: alternating observations of two close sources to determine the accuracy of the phase transfer and subsequent image errors; (3) *Go/noGo tests*: development of an online method to determine the near real-time feasibility of long baseline observations (Section 3.2); (4)
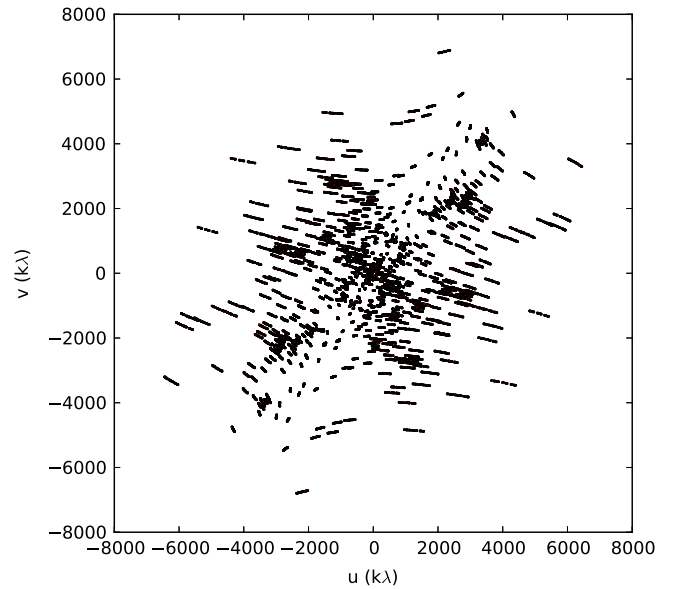
cycle time tests: phase referencing tests with different intervals between calibrator scans; (5) *baseline determination:* observations of many quasars distributed over the sky for 30 to 60 minutes to determine antenna positions and delay model (DM) errors; (6) *weak calibrator survey:* measuring the flux density of candidate calibrators for suitability as phase reference sources; (7) *calibrator structures:* imaging of calibrators at long baselines to search for significant angular sizes; and (8) *astrometry:* phase referencing among many close quasars to measure the long baseline source position accuracy.

Most test observations were made at 100 GHz (ALMA Band 3). The observed phase fluctuations are associated with variations in propagation time (delays) in the ALMA system or in the atmosphere, which are also described as path-length variations. The propagation changes are generally non-dispersive so that the phase fluctuations will scale with frequency[44] (although there are significant dispersive effects in the contributions due to water vapor at some frequencies above 350 GHz; these effects can be estimated).

3. SHORT-TERM COHERENCE

Imaging using phase referencing techniques requires a reasonably phase-stable array. Hence, an early goal of the LBC was to determine the short-term (5–60 s) phase rms properties of ALMA over a variety of conditions. In addition to phase noise, systematic phase offsets between the science target and calibrator were found; in Section 4, we describe their origin and how they were minimized.

One of the main contributions to phase instability at mm wavelengths is the fluctuation of the amount of water vapor in the atmosphere. The ALMA site was chosen for its low average water vapor content and excellent phase stability. Nevertheless, at baselines longer than 1 km, the short-term phase variations

---

[44] A useful conversion is that a path length change of 1 mm will produce a path delay change (assuming propagation at c) of 3.3 ps. The 1 mm path length change will produce a phase change of 120° at 100 GHz (Band 3), 300° at 230 GHz (Band 6), and 420° at 340 GHz (Band 7).

may make imaging impossible. A good rule of thumb is that if the rms phase variations are σ (rad), then the approximate loss of coherence (the decrease of the peak intensity of a point source caused by these random phase fluctuations) is $\exp[(-\sigma^2/2)]$ (Richards 2003). For $\sigma = 30°$ or $60°$ the coherence is respectively 87% or 58%. Hence, a general guideline is that the loss of coherence is acceptable and reasonably accurate image quality can be obtained if the rms phase fluctuations are <30°.

3.1. Water Vapor Radiometer Correction and the Spatial Structure Function

To estimate the path variations associated with the water vapour component, each antenna is equipped with a water vapor radiometer (WVR). The WVR is a multi-channel receiver system (Emrich et al. 2009) that makes continuous observations of the emission in the wings of the 183 GHz water line along the line of sight to the astronomical source. A description of this system, and of the way in which the measurements are used to estimate the variations in the amount of Precipitable Water Vapor (PWV)[45] in the path to each antenna, is given in Nikolic et al. (2013). This WVR correction typically removes about half the short-term phase fluctuations, and increases the proportion of time that phase referencing observations will produce good quality images. Even in good conditions, however, applying a correction to the phases based on these estimates still leaves residual fluctuations that are much larger than the estimated errors (which, with clear skies and PWV < 2 mm are believed to be less than 20 microns, although they can be much larger when clouds of ice or liquid water are present); see Figure 3. These residuals are thought to be mainly due to dry atmosphere (i.e., density) fluctuations (also see Section 4.2).

The properties of the phase rms as a function of baseline length are important for deciding when and how to observe at long baselines. Figure 3 shows a typical relationship of the phase rms, σ, as a function of baseline length, b, for a target at three stages of analysis. The σ–b relationship is called the spatial structure function (SSF). The characteristic shape is similar for both the uncorrected data and for the WVR corrected data, except for the decrease of the variations by about 50%. For short baselines, the rms phase increases as $\sigma \approx b^{0.83}$, indicative of a 3D Kolmogorov spectrum (Carilli & Holdaway 1999). The slope then decreases to a 2D Kolmogorov spectrum with dependence $\sigma \approx b^{0.33}$ at about 3 km, which is roughly the scale height of phase turbulence. This scale height is an average of the wet atmosphere and dry atmosphere scale sizes of 1 and 5 km at the ALMA site.

After phase referencing, the shape of the SSF is altered, as shown by the orange points in Figure 3. In this example, the calibrator is only 1°.3 away from the target, the cycle time is 20 s and the integration time on the calibrator is only 6 s. Only a small fraction of calibrators are sufficiently strong, even at Band 3, to provide adequate signal-to-noise (S/N) for accurate phase referencing calibration in this short integration time. Even in the ideal case of a sufficiently strong calibrator, for baselines less than 1 km, there is little decrease in the target rms after phase referencing. However, beyond a baseline of about 1 km, the target rms becomes less dependent on baseline length since the phase fluctuations with scale sizes greater than 1 km

---
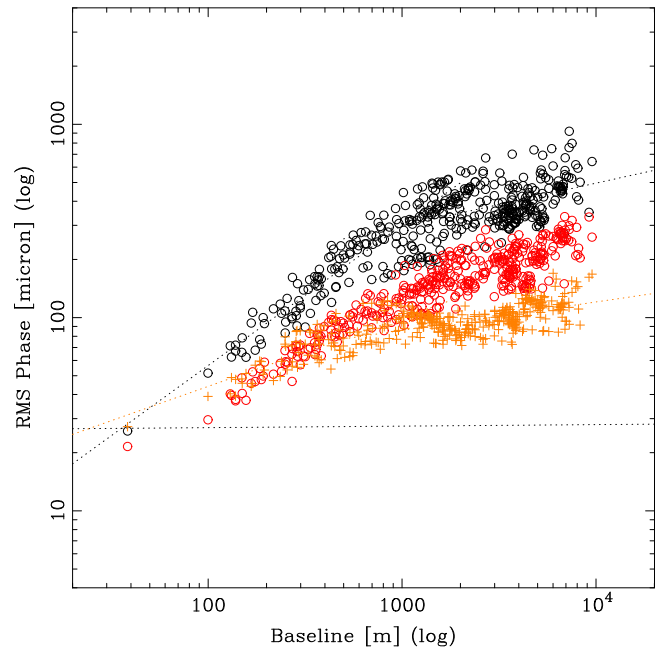
Figure 3. The spatial structure function (SSF). The phase rms (square-root of the SSF; converted to a path length in microns; see footnote 44) vs. baseline length is shown for a target at three stages of reduction. The experiment was 15 minutes in duration. The black points show the SSF for the original visibility data. The red points show the SSF points after applying the WVR correction for this source. The orange points show the SSF for this source *after* phase referencing with a calibrator that is 1°.3 away from the target with a cycle time of 20 s. The PWV during this experiment was 1.44 mm with a wind speed of 7 m s^{-1}.

are well correlated between the target and calibrator with a 20 s switching cycle time.

3.2. Go/noGo System

At the beginning of the campaign, it was hoped that the properties of the rms phase fluctuations (both before and after WVR correction) could be predicted from measurable weather parameters such as the average PWV, PWV rms, wind speed, and pressure rms. If so, then algorithms associated with these measured conditions could be used to indicate in advance if the phase parameters are adequate for imaging at a specified frequency; namely, that the short-term phase rms would be less than about 30° for the longer baselines. This presumption, however, turned out to be not always true.

A direct method to determine the current ALMA phase rms is from a short observation of a strong source. A simple observing procedure called *Go/noGo* was developed, consisting of a 2 minute observation of a strong quasar at Band 3, followed by online data analysis that rapidly determines the SSF with the WVR correction applied. To confirm that the *Go/noGo* structure function phase rms (averaged over many baselines between 5 and 15 km) is well correlated with phase referencing image quality, many *Go/noGo* observations that were carried out during the LBC were followed by short reference observations of calibrator-target pairs, with a typical 3°.5 separation and cycle time of 60 s. The plot of the *Go/noGo* rms phase versus image coherence from the phase referencing experiment is shown in Figure 4. This demonstrates that the target image coherence is reasonably well correlated with the rms phase at the longer baselines of the calibrator. The reason
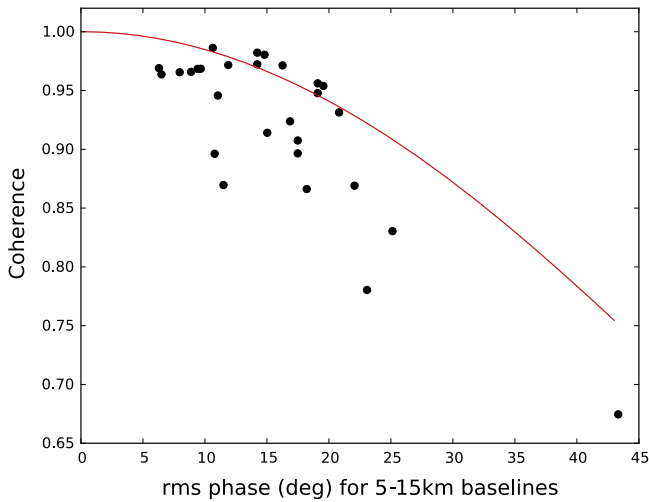
Figure 4. Average phase rms for 5–15 km baselines vs. coherence. The rms phase was determined from a set of *Go/noGo* (see Section 3.2) observations that were followed by short phase referencing experiments. The coherence is the ratio of the phase referenced image peak density divided by the self-calibrated image peak flux density. The thin red line shows the theoretical relationship between the phase rms (radians), σ, and coherence, i.e., $\exp(-\sigma^2/2)$ for a random phase distribution (see Section 3).

for the somewhat lower image coherence than expected from the rms phase variations are discussed in Section 4.

4. SYSTEMATIC PHASE ERRORS

In addition to the stochasticlike phase variations between the calibrator and target described in Section 3, there were systematic antenna-based phase offsets between the calibrator and science target that persisted on timescales of many minutes to hours. These were found to be caused mostly by errors in the correlator DM. The offsets were found to scale roughly as the calibrator-target separation, but were nearly unaffected by the cycle time. Such systematic offsets can have serious impact on the target image quality because they are persistant and produce image artifacts (e.g., large side-lobes and spurious faint components), in addition to the blurring of the target image that is associated with short-term phase fluctuations.

4.1. The Delay Model

The signals from all antennas must be combined precisely in phase at correlation to obtain accurate visibility phases. A critical part of the ALMA online control software, called the delay server, calculates the expected relative delay of the signals between each antenna from the ALMA array parameters (Marson et al. 2008). If the DM (which is calculated using the CALC[46] third-party software) is accurate, the visibility phase for any pointlike quasar with known position should be constant with time and independent of the quasar's position in the sky.

An important part of the DM is the estimate of the differential tropospheric delay between each antenna from the source. As described above, the wet delay component is calculated from the 183 GHz emission assuming a model temperature profile, and is included in the DM using the WVR measurement. The zenith dry air delay τ_i above antenna i is

accurately given by $\tau_i \approx 0.228 P_i$ where P_i is the dry pressure in mbars at the antenna (Thompson et al. 2001). For an observation of a target at elevation e, the CALC model delay is $(\tau_i)/\sin(e)$. Given that only one weather station near the array center had so far been available at the time of the LBC[47] at ALMA, the estimate of the dry air delay at each antenna is not as accurate as desired. This inaccuracy results in antenna-based phase offsets that differ between a calibrator and science target and hence produce relatively constant phase offsets between them.

4.2. Measurement of Delay Model Errors

The presence of DM errors was suspected from the baseline observations that consisted of about 50–100 ten-second observations of quasars distributed over the sky.[48] Many such observations have been made in order to determine the accurate relative positions of the antennas which are frequently moved from one antenna pad to another as the ALMA configuration changes. The a priori antenna positions are usually more than 1 mm in error, so the baseline observations provide the data needed to update antenna positions, generally to an accuracy of about 50 microns. Over a few years, it was found that the measured position changes of fixed antennas between baseline calibration observations, separated by several hours to a few weeks, were often larger than 100 microns and sometimes well over 1 mm for unmoved antennas that were more than 1 km from the array center.

These apparent antenna position changes were traced to the implementation of the dry air delay term in the CALC DM. Figure 5 illustrates the results of an experiment on 2014 September 16 with two 30-minute baseline observations that confirmed the DM error for a 3.5 km baseline with a height difference of 100 m between the two antennas. One experiment used the DM in which the pressure at each antenna was set equal to that measured by the one sensor. After fitting for the best baseline, the residual fit, shown by the red points, contains a large residual phase versus elevation term. In the subsequent experiments, the pressure at each antenna was estimated using the approximate pressure lapse rate. After the best baseline fit to the data, the residual phase versus elevation is flat. Since some antennas in the long baseline array have a height difference from the array center of over 200 m, even larger systematic phase errors could be encountered.

Without a reasonable pressure estimate for each antenna, the target and phase will have a systematic offset that will only slowly change. For example, the residual phase between a calibrator at elevation 55° and a target at elevation 60° is about 110°; this phase offset is not removed by the phase referencing. After the September demonstration of the issue, the ALMA DM was updated to include an estimate of the pressure at all antennas using the lapse pressure rate and the height of the current single pressure monitor (as noted in Section 4.1, additional pressure monitors distributed across the array will be available in the future). This height-delay compensation is also used at the VLA (Fomalont & Perley 1999).

Even after the correction of the antenna height delay differences, additional baseline observations during the last part of the LBC still showed apparent antenna position offsets

---

[46] http://lacerta.gsfc.nasa.gov/mk5/help/calc_01.txt

[47] Installation and testing of several additional weather stations distributed over the array is planned for the end of 2015.
[48] http://legacy.nrao.edu/alma/memos/html-memos/alma503/memo503.pdf
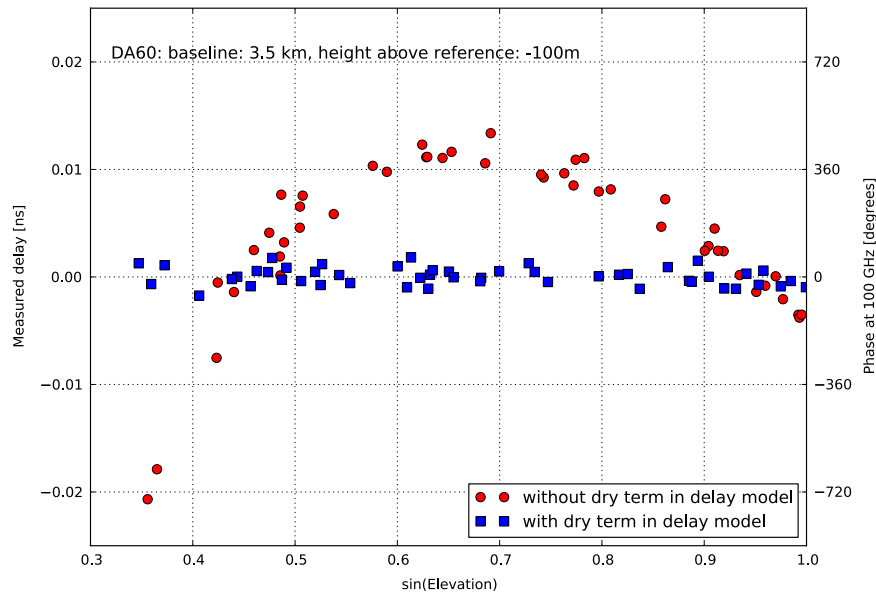
Figure 5. Effect of the height difference delay term. The residual delay/phase for one baseline (after fitting for the best antenna positions) is plotted vs. the sin (elevation) for 50 quasar scans that form a typical baseline observation. The baseline length is 3.5 km with an antenna height difference of 100 m. The red points show the residual delay/phases that used the nominal ALMA CALC delay model (Section 4.1) that assigned the measured pressure from the one weather station near the array center to *both* antennas. The blue points show the residual delay/phase for another baseline observation in which the estimated pressure for each antenna was estimated using the pressure lapse rate from the barometer near the array center.

of about 1–5 mm for most antennas 5–10 km from the center, which scaled roughly with distance from the array center. These apparent antenna position changes are consistent with the un-modeled pressure changes expected over the 15 km region of the Chajnantor plateau. However, by using a calibrator close to the target this effect is minimized; this requires a larger catalog of potential calibrators (Section 4.3).

Additional observational techniques can be employed to model the dry term delay residuals. For example, Very Long Baseline Array (VLBA) observations often include a short baseline-type observation (20 sources in 20 minutes) to determine the residual zenith path delay over each antenna (Reid & Honma 2014). Such options may be explored for future work.

4.3. The Weak Calibrator Survey and Calibrator Structure

To facilitate an optimal calibrator choice for a science target, most observatories support a source catalog that contains information about candidate calibrators. The ALMA calibrator catalog[49] in 2014 September contained 700 entries of quasars with positional accuracy <2 mas from Very Long Baseline Interferometry (VLBI) observations and with a 100 GHz flux density >25 mJy. Over the ALMA sky between −90° and +45° declinations, the mean angular distance of an ALMA catalog entry from a random target is 3°.5 with a 25% chance that the closest calibrator is >5° away. The number of suitable calibrators in the catalog, especially for the long baseline observations, therefore needed to be substantially increased. To this end, a survey of weak calibrators was initiated in mid-September to observe candidate sources from the Australia Telescope 20 GHz (AT20G) Survey (Murphy et al. 2010)

sample from Massardi et al. (2011) and the VLA calibrator catalogs[50] to determine their flux densities at 100 GHz. This list of 4200 candidate sources was compiled from sources potentially stronger than 25 mJy at 100 GHz, and observations prioritized the ~3000 sources with VLBI positions[51] having a positional accuracy of <2 mas. Sources as faint at 10 mJy at Band 3 may potentially be used as phase calibrators, but finding the faintest acceptable calibrators will probably require future targeted searches around a source.[52]

About 20 of the brightest ALMA calibrators were also imaged with the LBC array to determine if they were resolved at the longer baselines. Since most of the sources have been previously imaged using VLBI baselines of 5000 km at cm-wavelengths and found to be less than about 5 mas in angular size, it was expected that these calibrators would be nearly unresolved sources at ALMA long baseline resolutions. Two of the 20 sources, however, had faint inner jets whose brightness was a few percent of the bright core point component, but this structure has little effect on their use as calibrators of amplitude and phase on long baselines. A few of the brighter calibrators were already known to have large arcsecond-scale structures (J0522–3627 and 3C 273); this also has no significant effect on their use as long baseline calibrators.

4.4. Astrometric Accuracy

During the campaign, many hour-long experiments, cycling among three or four quasars within a radius of 10°, were carried out. All of the quasars have an a priori position accuracy of <0.3 mas, and were observed sequentially with 1 minute scans at Band 3. Using one of the quasars as the phase reference calibrator, images of the other quasars were obtained and the

[49] https://www.eso.org/sci/publications/messenger/archive/no.155-mar14/messenger-no155.pdf, page 19.

[50] http://www.aoc.nrao.edu/~gtaylor/csource.html
[51] http://astrogeo.org/vlbi/solutions/rfc_2015b/rfc_2015b_cat.txt
[52] https://science.nrao.edu/facilities/alma/aboutALMA/Technology/ALMA_Memo_Series/alma493/memo493.pdf/

Table 1
Long Baseline Astrometric Results

Source	J0538–4405[a]	J0519–4546	J0455–4615	J0522–3627		
Sep (Deg)	0.0	3.8	7.9	8.2		
rms (mas)[b]	0.13	0.20	0.35	0.08		
DATE	R.A., Decl. Offset (mas)				PWV(mm)	ELEV(deg)
Sep 22	−0.45, +0.15	−0.44, −2.20	+11.0, −2.96	+0.48, +1.82	0.7	66
Oct 03	−0.09, −0.10	+0.28, −4.57	+4.03, −8.14	+1.32, −2.99	2.7	71
Oct 14	+0.06, +0.08	−2.69, +0.25	…	+0.74, −3.49	0.6	55
Oct 14	−0.00, −0.03	+0.54, +1.27	+8.81, +3.84	−4.00, −1.70	0.9	71
Nov 04	−0.03, −0.02	−0.21, +2.12	+7.08, +4.80	−4.60, +0.60	0.9	48
Nov 17	−0.01, +0.05	−2.72, −1.24	−6.56, −1.96	−9.02, −0.17	1.3	66
Mean	−0.09, +0.02	−0.87, −0.73	−4.87, −0.88	−2.51, −0.99	…	…
STD (Mean)	0.08, 0.03	0.54, 0.92	2.75, 2.15	1.15, 0.78	…	…

Notes. Details are given in Section 4.4.
[a] Phase reference source.
[b] Theoretical rms, defined as the angular resolution divided by the theoretical S/N, where the latter is derived from the peak flux density of the source divided by the expected image rms noise level.

positional offset for each source was determined by the displacement of the quasar peak from the center of the image. Uniform weighting with only spacings longer than 1 km were used to obtain the highest resolution and most accurate positions.

The results for the same quartet of quasars observed six times over the LBC are given in Table 1. The source J0538–4405 is the phase reference source, so its position should be close to zero. The separation of the sources from J0538–4405 in degrees and the theoretical positional rms error in mas are listed in the first two rows. The subsequent rows then give the R.A. and decl. offset for each source for each of the six observations, with the mean positional offset and the standard deviation of the mean at the bottom. The results show that the positional offsets of the three target sources are significantly larger than those expected from the image noise alone (typically ∼1–5 mas). The source, J0519–4546, closest to the phase reference source, shows the smallest systematic offset (∼0.8 mas). The other two sources, one to the east and one to the south of J0538–4405, have larger offsets. This relationship is consistent with that produced by the relatively systematic atmospheric DM errors discussed in Section 4.2. In the future, it will be possible to use the apparent positional offsets of three calibrators to determine more information about the DM error over the array, and then remove the errors to obtain more accurate positions of the calibrators. Such multi-calibrator observations and analyses have proved successful with the VLBA for significantly improving the astrometric precision (Fomalont & Kopeikin 2002) and are now being tested for ALMA.

The nominal astrometric accuracy from the LBC tests, given by the average rms in Table 1 for the three sources, is an rms positional error of ∼1.5 mas. This is for an average calibrator-target separation of ∼ 6°, with an observing period of one hour, with a maximum baseline of 12 km. Given a sufficiently strong point source, this accuracy is independent of observing frequency. The predicted ALMA astrometric accuracy is ∼0.18 mas (Lestrade 2008), assuming the use of WVR corrections and a typical calibrator-target separation of 6° (which is within the range used in the LBC). However, this predicted value assumes that the pressure measurement at each antenna would be accurate to ±2 mbars. As discussed in Section 4, with the availability of only one weather station during the LBC, the inferred pressure

for antennas many kilometers from the pressure sensors, using a simple plane-parallel atmosphere model and lapse rate, could be in error by tens of mbars. This produces a systematic phase error between calibrator and target and is likely the major cause of the poorer than expected astrometric accuracy observed during the LBC. It is expected that the addition, in late 2015, of more weather stations distributed over the array will improve the astrometric accuracy.

5. SCIENCE VERIFICATION

SV is the process of fully testing observing modes expected to be available for science observing by making end-to-end observations (e.g., execution of scheduling blocks, calibration, and imaging) of a small number of selected astronomical objects. The aim is to demonstrate that ALMA is capable of producing data of the quality required for scientific analysis so that the observing mode can be offered for future science observations. To demonstrate ALMA's high angular resolution capability, during the LBC we carried out SV observations of five targets chosen from a broad range of science areas (Table 2). The aim was to produce high-fidelity, high-resolution images of continuum and spectral line emission using the LBC array.

The SV targets were chosen primarily based on their suitability for demonstrating the long baseline capability, e.g., having fine-scale angular structure, being <2″ in angular size, being observable at night-time during the campaign period, and, where possible, having previous observations with other telescopes. The targets were Juno, an asymmetric asteroid with a 7.2 hr rotation period; Mira, a well-studied AGB star that is the prototypical Mira variable; HL Tau, a young star with a circumstellar disk; 3C 138, a strongly polarized extended quasar; and SDP.81, a high-z ($z = 3.042$), gravitationally lensed, submm galaxy. Details of the targets and observations are given in Table 2 and the data are publicly available from the ALMA Science Portal.[53] Examples of the SV imaging results are given in three accompanying papers on targets HL Tau, Juno, and SDP.81 (ALMA II; ALMA III; ALMA IV). Angular resolutions achieved were as fine as 19 mas (Band 7; 344 GHz; ALMA III). In Appendix A, we compare preliminary ALMA

---
[53] http://www.almascience.org

Table 2
ALMA Long Baseline Science Verification Targets

Target	Coordinates[a]	Band[b]	Scope[c]	N_{ant}[d]	N_{ex}[e]	t_{ON}[f]	Frequency[h]	Obs. Date[i]	Id.[j]
Juno	ephemeris target	6	cont., ephemeris	30–33	5	0.3[g]	224.0, 226.0, 240.0, 242.0	Oct 19	13
Mira	$02^h19^m20\overset{s}{.}79$ $-02°58'39\overset{''}{.}5$	3	SiO, cont.	31–33	3	1.5	88.2, 98.2, 100.2, 86.8, 86.2, 85.6, 85.7	Oct 17–Oct 25	14
		6	SiO, cont.	35–36	3	1.0	229.6, 214.4, 214.1, 215.6, 217.1, 232.7, 231.9	Oct 29–Nov 01	14
HL Tau	$04^h31^m38\overset{s}{.}45$ $+18°13'59\overset{''}{.}0$	3	CO, CN, cont.	32–35	7	3.2	102.9,101.1,115.3,113.5	Oct 28–Nov 14	15
		3	HCN, HCO+, cont.	33–35	7	3.5	90.8,100.8,102.8,88.6,89.2	Oct 14–Nov 13	15
		6	cont.	28–36	9	4.7	224.0,226.0,240.0,242.0	Oct 24–Oct 31	15
		7	cont.	27–36	10	5.1	336.5,338.4,348.5,350.5	Oct 30–Nov 06	15
3C 138	$05^h21^m09\overset{s}{.}9$ $+16°38'22''$	3	cont., polarization	27–30	6	2.0	90.5, 92.5, 102.5, 104.0	Nov 10–Nov 19	...
		6	cont.	29–31	5	1.6	224.0, 226.0, 240.0, 242.0	Nov 09–Nov 14	...
SDP.81	$09^h03^m11\overset{s}{.}61$ $+00°39'06\overset{''}{.}7$	4	CO, cont.	22–27	12	5.9	144.6,154.7,156.4,142.7	Oct 21–Nov 11	16
		6	CO, H_2O, cont.	30–36	9	4.4	228.0, 230.0, 243.0, 244.5	Oct 12–Nov 09	16
		7	CO, cont.	31–36	11	5.6	282.9, 294.9, 296.9, 284.9	Oct 30–Nov 04	16

Notes. Further details of the Juno, HL Tau, and SDP.81 observations and results are given in three accompanying papers (ALMA II; ALMA III; ALMA IV). The data are publicly available from the ALMA Science Portal (see footnote 53).
[a] Coordinates of the phase center (J2000).
[b] ALMA Bands. Bands 3, 4, 6, and 7 correspond to frequencies of approximately 100, 140, 230, and 340 GHz, respectively.
[c] Scope and aim of the observations. These include spectral line and/or continuum imaging at high angular resolution, plus polarization and ephemeris targets.
[d] Number of antennas in the array for each execution. Typically, between 1 and 5 of the total number of antennas were flagged for a given execution. Note that the number and configuration of the antennas on very short spacings varied from day to day (see Section 2). The number of antennas also varied with observing Band, with the fewest antennas available in Band 4 (due to fewer antennas with Band 4 receivers available during the LBC).
[e] Total number of executions of the scheduling block.
[f] Total effective integration time on source (i.e., after flagging), in hours.
[g] For specific details of Juno, see ALMA II.
[h] Mean center frequency of each spectral window (spw) in GHz. Channel widths were 15.6 MHz for continuum windows, with 2.0 GHz bandwidth per spw. Channel widths varied for spectral line windows. For Mira, they were 61–122 kHz, with 0.059–0.117 GHz bandwidth. For HL Tau, they were 61 kHz, with 0.117 or 0.243 GHz bandwidth. For SDP.81, they were 0.488–1.953 GHz, with 1.875 GHz bandwidth.
[i] Range of dates of the observations.
[j] The project code identifier of the data set can be obtained by replacing "XX" in ADS/JAO.ALMA#2011.0.000XX.SV with the number in this column.

results on 3C 138 with a 43 GHz VLA image. Details of the imaging of the SV targets, including important lessons learned, are described in a CASA guide page.[54] Specific comments concerning the use of self-calibration to improve image quality are given in Appendix B.

6. CONCLUSIONS

The 2014 ALMA LBC achieved an increase of a factor of ∼6 in maximum baseline length (∼15 km) compared to previous test observations and a factor of ∼10 increase compared to previous ALMA science observations (a factor of ∼100 smaller beam area). Further testing will be carried out in the future to extend the capability to a maximum baseline of ∼16 km and to higher frequencies.

Some specific results drawn from the campaign are as follows.

1. Phase referencing observations should only be made when the short-term phase rms is <30°, unless the target source is relatively compact and strong enough for self-calibration. This applies to all ALMA observations, regardless of maximum baseline length or frequency.
2. Under clear skies, the WVR correction typically improves the phase noise by a factor of ∼2. The remaining phase fluctuations are thought to be mostly due to dry atmosphere variations.

3. The prediction of short-term phase variability cannot be made reliably using ground-based measurements. Short observations of a strong source are the most reliable methods to determine phase conditions, as described in the *Go/noGo* procedure.
4. Systematic phase differences between calibrator and science target are dominated mainly by the lack of an accurate dry atmospheric delay model. Additional pressure sensors distributed across the ALMA array will improve the models in the future.
5. The phase referencing cycle time recommended for long baseline observations is 60–90 s between calibrator observations. Shorter times do not significantly improve the image quality unless a calibrator <1°.5 from the target is sufficiently strong that it can be detected with a 6 s integration.
6. The survey of weak calibrators will continue in order to increase the number of sources in the catalog and increase sky coverage. Alternative calibrator observing strategy may be needed in future in order to find the faintest acceptable calibrators.
7. The integration time on source may in many cases be driven by the time needed to obtain sufficient *uv*-coverage, rather than that needed to reach a specified rms. In the future, detailed simulations may be needed to investigate this.
8. More sophisticated methods of self-calibration may be needed for extended sources where the S/N on the longer

---

[54] http://casaguides.nrao.edu/index.php?title=ALMA2014_LBC_SVDATA

baselines drops below that needed for self-calibration using one reference antenna.

As a result of the extensive program of testing during the LBC, SV at long baselines was highly successful, resulting in angular resolutions as fine as 19 mas. Initial science results on the SV data are presented in ALMA II, ALMA III, and ALMA IV. The LBC has allowed long baseline (up to ~15 km) antenna configurations to be made available for science observations. This fulfills a major goal of ALMA to accurately image sources at mm and submm wavelengths with resolutions of tens of milliarcseconds, and, together with ALMA's high sensitivity, opens up new parameter space for submm astronomy.

This paper makes use of the following ALMA data: ADS/JAO.ALMA#2011.0.00013.SV, ADS/JAO.ALMA#2011.0.00014.SV, ADS/JAO.ALMA#2011.0.00015.SV, and ADS/JAO.ALMA#2011.0.00016.SV. ALMA is a partnership of ESO (representing its member states), NSF (USA) and NINS (Japan), together with NRC (Canada), NSC and ASIAA (Taiwan), and KASI (Republic of Korea), in cooperation with the Republic of Chile. The Joint ALMA Observatory is operated by ESO, AUI/NRAO and NAOJ. The National Radio Astronomy Observatory is a facility of the National Science Foundation operated under cooperative agreement by Associated Universities, Inc. We thank all those who have contributed to making the ALMA project possible.

Facility: ALMA.

APPENDIX A
ALMA OBSERVATIONS OF 3C 138

The source 3C 138 = J0521+1638 is a compact steep spectrum quasar with $m_v = 18.84$ and a redshift of 0.759 (Cotton et al. 1997). Its angular size is about 0″.4 and consists of a radio core, with a strong jet/lobe to the east and a weaker counter-lobe to the west. The integrated source linear polarization is 10% and its total flux density is relatively stable.

The source 3C 138 was chosen as an SV target because its angular size and small-scale structure are ideal for imaging with the ALMA long baselines, it is a highly polarized target, and the ALMA resolutions at Band 3 and Band 6 with a 5–15 km baseline array are comparable to that of the VLA 35 km baseline array at 43 GHz. Thus, a detailed comparison of the images made with different arrays can be made. For the other LBC SV targets, the ALMA resolution and sensitivity far exceed those of other arrays so any detailed comparison cannot be made. Hence, the discussion here will concentrate on ALMA–VLA comparison, rather than any astrophysical interpretations. The analysis of the complete set of 3C 138 ALMA observations (with full polarization) is in progress. Here, we present preliminary results.[55]

The ALMA observation parameters for Bands 3 and 6 are listed in Table 2. The VLA observations at 43 GHz were made on 2014 February 16 in the A-configuration, and the integration time on 3C 138 was 45 minutes. The VLA observations used J0530+1331 as the phase calibrator, while the ALMA observations used J0510+1800, both of which are within 4° of 3C 138. The flux density scale for ALMA was based on the

derived flux density of 1.20 Jy and 0.97 Jy (10% uncertainty) for J0510+1800 at 97 and 241 GHz, respectively. For the VLA, the source 3C 48 was used for the flux density scale. The phase referencing cycle time was 95 s for ALMA and 90 s for the VLA.

The standard phase referencing calibration, editing, imaging, and self-calibration for the ALMA and VLA data were carried out using the *obit*[56] software package (Cotton 2008). Since the structure of 3C 138 is dominated by a small component, the self-calibration process was straight-forward. In order to compare the images at the three frequencies at the same resolution (91×51 mas in P.A. 13°), each data set was weighted to include approximately the same range of spacings for each image, and then convolved with the above Gaussian beam size.

The preliminary ALMA 97 & 241 GHz and VLA 43 GHz images are shown in Figure 6. The bright, compact radio core and strong eastern jet and lobe, respectively, have spectral indices of -0.70 ± 0.03 and -0.75 ± 0.05. The western counter-jet, which is severely Doppler attenuated, is weak and has a spectral index of -0.95 ± 0.13; its peak is just below the 3 rms intensity level at 241 GHz. The lowest contour level for all three images is 0.5% of their peak intensity (3 times rms), so that the peak to rms ratios for these images are about 500:1. The main conclusion is that the differences between the ALMA and VLA images are at the level of a few percent of their peak levels. The two arrays have major differences, such as their antenna, electronics, and correlator designs; the atmospheric conditions; and ALMA linear polarized feeds versus the VLA circular polarized feeds. Hence, the agreement of the images to a few percent strongly suggests that both arrays can image the radio emission from the sky at tens of milliarcsecond resolution with this accuracy or better.

The ALMA Band 6 image using the high-resolution data at natural weight is shown in Figure 7. The resolution is 37×23 mas in P.A. $-11°$, which is considerably higher than that used for the three-frequency comparison. At this higher resolution, the western jet has broken into six knots and an inner jet emanating east from the core can be separated. The jet/lobe system has a slight curvature, which is also seen on VLBA images of this source (Cotton et al. 2003). The faint western counter-jet has a peak flux density of 0.25 mJy, just below the lowest contour level at 0.3% of the peak.
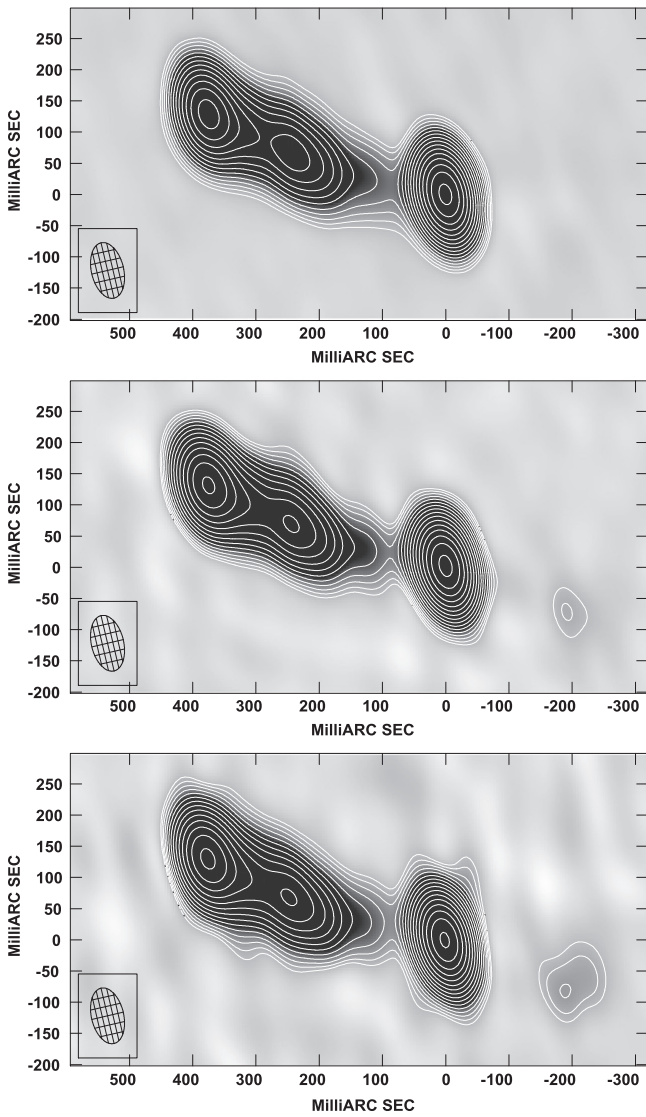
APPENDIX B
SELF-CALIBRATION

Some of the SV targets were sufficiently strong enough that self-calibration could be used to improve the image quality over that obtained with phase referencing alone. The Juno images (ALMA II) were significantly improved with self-calibration and obtained a peak/image rms of typically 120 for each of the nine images, providing an increase over the phase-referenced only images of a factor of two to six.

For the HL Tau continuum images (ALMA III), self-calibration was more challenging because while the overall integrated flux is large, the source morphology is complex. Indeed, much of the disk emission is resolved out by the longest baselines, especially at Band 7, and for the lower

---

[55] The ALMA Band 3 and 6 average frequencies for the initial results presented here are respectively 97 and 241 GHz; only the upper sideband of the Band 6 data was used.
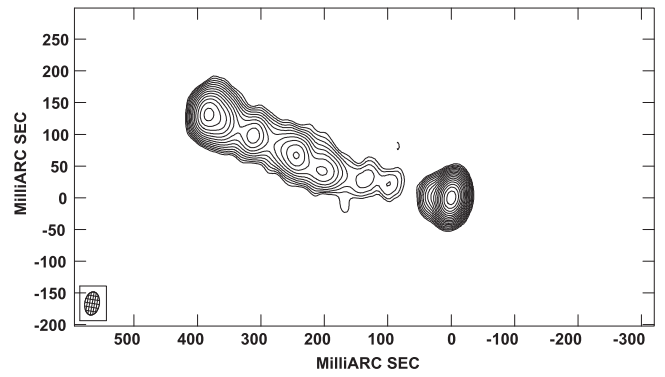
[56] Note that the ALMA data could have been processed in CASA 4.2.2 or higher, but was done in *obit* for consistency with the previously reduced VLA data.

Figure 7. Highest-resolution ALMA image of 3C 138 at 241 GHz. The resolution is 37×23 mas at P.A. $= -11°$ (shown by the cross-hatched ellipse). The contour levels are in multiplicative increments of $\sqrt{2}$. The peak flux is 0.095 Jy beam^{-1} and the lowest contour is 0.33% of the peak.

decreases about a factor of 10 from the phase referenced to the self-calibrated image. A conservative measure is the ratio of the highest side-lobe level to the peak intensity. For the 97 GHz image, the side-lobe/peak intensity ratio drops from 1.4% in the phase referenced image to 0.1% in the self-calibrated image. For the 241 GHz image, the ratio drops from 17% to 0.6%.

One particular complication of self-calibration at long baselines is that unless the target structure is already well studied at high resolution, only a rough estimate of its correlated flux density at the longer baseline may be estimated. Therefore, in many cases it may be difficult to predict in advance whether a given source can be self-calibrated on the longest baselines. In the future, more sophisticated methods of self-calibration may benefit extended sources where the S/N on the longer spacings drops below that needed for self-calibration using one reference antenna. Furthermore, future testing on long baselines will provide further insight into ALMA long baseline imaging and self-calibration.

REFERENCES

ALMA Partnership, Hunter, T. R., Kneissl, R., et al. 2015a, ApJL, 808, L2 (ALMA II)
ALMA Partnership, Brogan, C. L., Perez, L. M., et al. 2015b, ApJL, 808, L3 (ALMA III)
ALMA Partnership, Vlahakis, C., Hunter, T. R., et al. 2015c, ApJL, 808, L4 (ALMA IV)
Asaki, Y., Matsushita, S., Kawabe, R., et al. 2014, Proc. SPIE, 9145, 91454K
Beasley, A. J., & Conway, J. E. 1995, in ASP Conf. Ser. 82, Very Long Baseline Interferometry and the VLBA, ed. J. A. Zensus, P. J. Diamond, & P. J. Napier (San Francisco, CA: ASP), 327
Carilli, C. L., & Holdaway, M. A. 1999, RaSc, 34, 817
Cotton, W. D. 2008, PASP, 120, 439
Cotton, W. D., Dallacasa, D., Fanti, C., et al. 1997, A&A, 325, 493
Cotton, W. D., Dallacasa, D., Fanti, C., et al. 2003, A&A, 406, 43
Emrich, A., Andersson, S., Wannerbratt, M., et al. 2009, in Twentieth International Symposium on Space Terahertz Technology ed. E. Bryerton, A. Kerr, & A. Lichtenberger, 174
Fomalont, E. B., & Perley, R. A. 1999, in ASP Conf. Ser. 180, Synthesis Imaging in Radio Astronomy II, ed. G. B. Taylor, C. L. Carilli, & R. A. Perley (San Francisco, CA: ASP), 79
Fomalont, E. B., & Kopeikin, S. 2002, in Sixth European VLBI Network Symposium on New Developments in VLBI Science and Technology, ed. E. Ros, R. W. Porcas, A. P. Lobanov, & J. A. Zensus (Bonn: Max-Planck-Institut für Radioastronomie), 53
Lestrade, J.-F. 2008, in IAU Symp. No. 248, A Giant Step: from Milli- to Micro-arcsecond Astrometry, ed. W. J. Jin, I. Platais, & M. A. C. Perryman (Cambridge: Cambridge Univ. Press), 170

Figure 6. Images of 3C 138 with 91×51 mas resolution and P.A. 13° (as shown by the cross-hatched ellipse). (top) ALMA image at 241 GHz with a peak flux of 0.235 Jy beam^{-1}. (middle) ALMA image at 97 GHz with a peak flux of 0.235 Jy beam^{-1}. (bottom) VLA image at 43 GHz with a peak flux of 0.387 Jy beam^{-1}. For all images the lowest contour is 0.5% of the peak and the contour levels are in multiplicative increments of $\sqrt{2}$. Details of the images are given in Appendix A.

frequency bands the emission is intrinsically weaker due to the lower dust emissivity. Thus, the S/N for self-calibration is inadequate for the longest baseline antennas if one attempts to push to short enough timescales (less than a few minutes) to significantly improve the phases beyond that achieved from fast-switching. Due to this S/N limitation on the solution interval, the self-calibration only improves the HL Tau images (peak/rms) by factors of 1.5, 1.9, and 1.2 at Bands 3, 6, and 7, respectively. For the much weaker source SDP.81, there is inadequate S/N to self-calibrate on a short enough timescale to improve the images at all (while retaining the longest baseline antennas).

Since the 3C 138 emission is dominated by a nearly unresolved core and the remaining structure is relatively simple, it showed the most improvement. The rms noise level

Marson, R., Kern, J., Farris, A., & Hiriart, R. 2008, Proc. SPIE, 7019, 701905
Massardi, M., Ekers, R., Murphy, T., et al. 2011, MNRAS, 412, 318
Matsushita, S., Asaki, Y., Kawabe, R., et al. 2014, Proc. SPIE, 9145, 9145311
Matsushita, S., Matsuo, H., Pardo, J. R., & Radford, S. J. E. 1999, PASJ, 51, 603
Murphy, T., Sadler, E. M., Ekers, R. D., et al. 2010, MNRAS, 402, 2403

Nikolic, B., Bolton, R. C., Graves, S. F., Hills, R. E., & Richer, J. S. 2013, A&A, 552, A104
Richards, M. A. 2003, ISPL, 10, 208
Reid, M. J., & Honma, M. 2014, ARA&A, 52, 339
Thompson, A. R., Moran, J. M., & Swenson, G. W., Jr (ed.) 2001, Interferometry and Synthesis in Radio Astronomy (2nd ed.; New York: Wiley)